Stress resultant intensity factors evaluation of cracked folded structures by 6DOFs flat shell meshfree modeling

S. Tanaka[a,*], M.J. Dai[a], S. Sadamoto[a,1], T.T. Yu[b], T.Q. Bui[c]

[a]*Graduate School of Engineering, Hiroshima University, Japan,*
e-mail: satoyuki@hiroshima-u.ac.jp, mingjyundai@gmail.com, shota.sadamoto@gmail.com
[b]*Department of Engineering Mechanics, Hohai University, China,*
e-mail: tiantangyu@hhu.edu.cn
[c]*Department of Civil and Environmental Engineering,*
Tokyo Institute of Technology, Japan, e-mail: bui.t.aa@m.titech.ac.jp

Abstract

Several numerical examples for cracked folded structures are analyzed to investigate the mixed-mode stress resultant intensity factors (SRIFs). The kinematic formulations of structures are derived by the first order shear deformation plate theory. A Galerkin meshfree six degrees of freedom (6DOFs) flat shell is employed, in which the reproducing kernel (RK) is used as the meshfree interpolant. A diffraction method, visibility criterion and enriched basis are introduced to model the through crack. J-integral is evaluated based on the stress resultants and is decomposed into the symmetric and asymmetric parts for extracting the mixed-mode SRIFs. Not only the stiffness matrix but also the J-integral are discretized by nodes. They are numerically integrated by the stabilized conforming nodal integration (SCNI) and the sub-domain stabilized conforming integration (SSCI) techniques. The effectiveness of the meshfree modeling and accuracy in the SRIFs are discussed.

Keywords: Folded Structure; Fracture; Meshfree Method; Nodal Integration; J-integral

---

[*]Corresponding author.
[1]Present address: Fujitu Limited, 9-3, Nakase 1-chome, Mihama-ku, Chiba city, Chiba 261-8588, Japan

1. Introduction

Evaluation of cracks or defects in shell structures is one of great importance in analyzing the structural integrity and reliability of thin-walled structures such as ship's hull, aircraft fuselage and pressure vessel [1-6]. Stress intensity factors (SIFs) are the fracture mechanics parameters in evaluating the mechanical behaviors of the damaged structures. A number of studies have been carried out to examine the SIFs in solids and structures due to significance of fatigue and fracture assessment. However, most of the studies dealing with fracture problems based on two-dimensional (2D) plane strain/plane stress condition and the three-dimensional (3D) continuum mechanics theory [7,8].

When treating fracture problems in shell structures, not only membrane but also bending deformations are taken into account for the structural analysis and the SIFs evaluation, see *e.g.*, Refs. [9-11] and references therein. A conventional modeling of a cracked shell structure such as the finite element method (FEM) often requires a special treatment of the shear locking problems. To offer high accuracy computation of the stress/strain components around the crack, fine meshes are also required to the conventional FEM simulation. So far, effective computational methods have been proposed to analyze the cracked plate and shell problems. Dolbow *et al.* [12] treated fracture problems in plates by employing MITC4 plate element and the extended FEM (XFEM) [13, 14]. Baiz *et al.* analyzed linear buckling analysis of cracked plates using smoothed FEM and XFEM [15]. Additionally, cracked functionally graded plates were analyzed for vibration problems by an 8-node shear flexible element [16] and XFEM [17]. Dirgantara and Aliabadi analyzed cracked shells by the dual boundary element method [18,19].

In the last two decades, meshfree methods [20-22], isogeometric analysis [23], wavelet Galerkin methods [24-28] and *etc.* have been developed and applied to the plate and shell problems [29-33]. Because continuous functions are adopted in the approximation of the plate and shell deformations, the methods can address the shear locking problem without special treatments in the formulation and discretization. The continuous stress/strain components are well suited for the fracture mechanics parameter evaluation.

The authors' previous study, structural analyses by meshfree method had been carried out. RKs [21] were adopted as the meshfree interpolant to approximate the membrane and plate bending deformations. Mindlin-Reissner plate theory, *i.e.*, first order shear deformation plate theory [34,35] was cho-

sen. The shear locking problem was addressed by imposing so-called Kirch-
hoff Mode Reproducing Condition (KMRC) [34]. A structure was discretized
by nodes. SCNI [36,37] and SSCI [38-43] were applied as numerical inte-
gration. The recent advance of SCNI/SSCI was presented, which are nest-
ing sub-domain gradient smoothing integration and RK gradient smoothing
framework [44,45]. So far, a flat shell with five degrees of freedom (5DOFs)
was developed for solving geometrical nonlinear analyses [46] and buckling
problems [47,48]. A singular kernel (SK) [49] was also adopted to impose
Kronecker delta property on the nodes for applying the essential boundary
conditions (BCs). In addition, to treat the folded geometry, a drilling DOF
was included. Buckling problems of stiffened plate structures were analyzed
using the 6DOFs flat shell [50,51].

In the present study, several numerical examples for cracked folded struc-
ture are analyzed and the mixed-mode SRIFs are evaluated using the effective
meshfree modeling. The folded structures are solved by the 6DOFs flat shell
formulation and discretization. A diffraction method, visibility criterion [52]
and enriched basis [53] are introduced to model the through crack. J-integral
is decomposed into the symmetric and asymmetric parts employing the stress
resultants for extracting the mixed-mode SRIFs. It is discretized by nodes
and is integrated numerically by SCNI and SSCI. A path independency in the
SRIFs is examined and the results are compared with the reference solutions
and commercial FEM software solutions. Although the authors developed
J-integral meshfree discretization technique in [54] and adopted for mem-
brane fracture problems [55] and bending fracture problems [56], there is no
adoption of cracked flat shell and cracked folded structure problems. Because
membrane deformation is dominant in the fracture problems, the membrane
SRIFs are only investigated in the fracture mechanics parameter evaluations.

The structure of the paper is follows. A meshfree flat shell formulation
and discretization for cracked folded structure is presented in Section 2. A
technique to evaluate the SRIFs for flat shell structures is presented in Section
3. Numerical examples are shown in Section 4. Conclusions are given in
Section 5.

2. Galerkin meshfree flat shell formulation and discretization

2.1. Galerkin meshfree flat shell formulation

A Galerkin flat shell formulation is employed and the RKs are adopted
as the meshfree interpolants for analyzing a linear elastic folded structure

3

problem including a through crack. A schematic of a cracked flat shell is presented in Fig.1(a). x_1-x_2-x_3 is chosen as a global coordinate system. The middle-section of the shell is assumed on x_1-x_2 plane, and x_3 ($-t/2 < x_3 < t/2$) is taken as normal direction of the x_1-x_2 plane. t is the shell thickness.
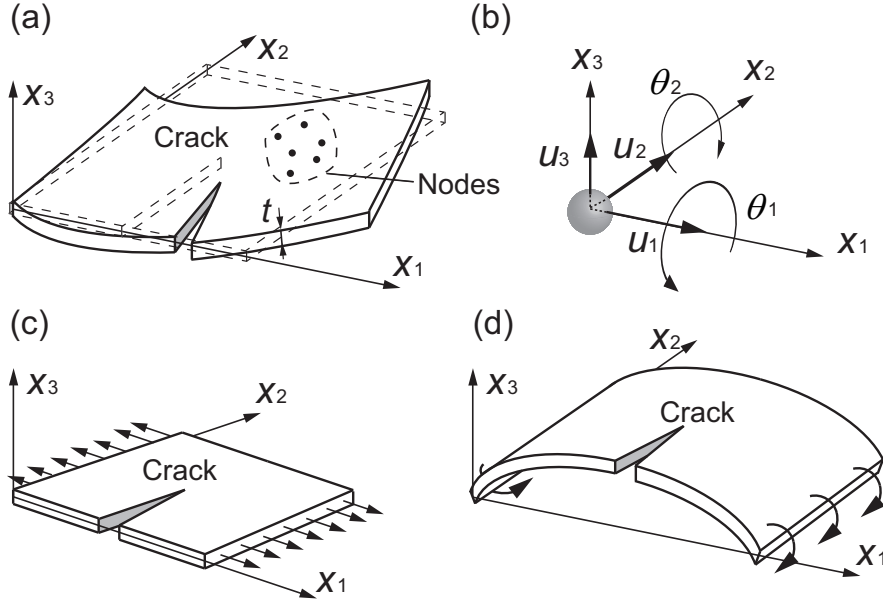

Figure 1: A cracked flat shell. [(a) A deformed cracked shell, (b) 5DOFs per node to approximate the shell deformation, (c) Membrane deformation, (d) Bending deformation]

The nodes are scattered on the middle-plane of the shell. Each node has 5DOFs as shown in Fig.1(b). There are two membrane deformation components (u_{1mid} and u_{2mid}) and three bending deformation components (u_3, θ_1, and θ_2) as shown in Fig.1(c) and (d), respectively. Where $u_{i\,mid}$ (i=1,2) are the displacement components of the x_i-direction. u_3 is the displacement component along x_3-direction. θ_i (i=1,2) are the rotation components in terms of the x_i-direction. The displacement vector in the flat shell $\boldsymbol{u}(\boldsymbol{x})$ at position $\boldsymbol{x}$ can be described, as:

$$\boldsymbol{u}(\boldsymbol{x}) = \left\{ \begin{array}{c} u_1(\boldsymbol{x}) \\ u_2(\boldsymbol{x}) \\ u_3(\boldsymbol{x}) \end{array} \right\} = \left\{ \begin{array}{c} u_{1mid}(\boldsymbol{x}) + z\theta_2(\boldsymbol{x}) \\ u_{2mid}(\boldsymbol{x}) - z\theta_1(\boldsymbol{x}) \\ u_3(\boldsymbol{x}) \end{array} \right\}, \tag{1}$$

where $u_i(\boldsymbol{x})$ (i=1,2,3) is the displacement components. z ($||z|| \leq t/2$) is taken as a coordinate along the shell thickness direction. The virtual work principle

for the flat shell is written as:

$$\int_{\Omega} \boldsymbol{\sigma} : \delta\boldsymbol{\varepsilon} \; d\Omega - \delta W = 0,$$

$$\delta W = \int_{\Gamma} \bar{\boldsymbol{p}} \cdot \delta\boldsymbol{u} \; d\Gamma + \int_{\Omega} \bar{q} \cdot \delta u_3 \; d\Omega + \int_{\Gamma} \bar{M}_{nn} \cdot \delta\theta_n \; d\Gamma, \qquad (2)$$

where $\delta\boldsymbol{u}=\{\delta u_1 \;\; \delta u_2\}^T$, δu_3 and $\delta\theta_n$ (n=1,2) are the variations corresponding to components of the displacements and rotations. Ω and Γ are the analysis domain and its boundary. $\bar{\boldsymbol{p}}$, $\bar{q}$, and $\bar{M}_{nn}$ are traction on the boundary, distributed pressure on the shell, and moment on the boundary, respectively. $\boldsymbol{\varepsilon}$ ($=\varepsilon_{ij}$) is a strain tensor. The components can be written as:

$$\varepsilon_{11} = \frac{\partial u_{1mid}}{\partial x_1} - z\frac{\partial\theta_1}{\partial x_1}, \quad \varepsilon_{22} = \frac{\partial u_{2mid}}{\partial x_2} - z\frac{\partial\theta_2}{\partial x_2},$$

$$2\varepsilon_{12} = \left(\frac{\partial u_{1mid}}{\partial x_2} - z\frac{\partial\theta_1}{\partial x_2}\right) + \left(\frac{\partial u_{2mid}}{\partial x_1} - z\frac{\partial\theta_2}{\partial x_1}\right),$$

$$2\varepsilon_{31} = \frac{\partial u_3}{\partial x_1} - \theta_1, \qquad 2\varepsilon_{23} = \frac{\partial u_3}{\partial x_2} - \theta_2. \qquad (3)$$

They are rewritten in a vector form, as:

$$\{\boldsymbol{\varepsilon}\} = \{\varepsilon_{11} \;\; \varepsilon_{22} \;\; \varepsilon_{12} \;\; \varepsilon_{31} \;\; \varepsilon_{23}\}^T. \qquad (4)$$

When $\{\boldsymbol{\sigma}\}=\{\sigma_{11} \;\; \sigma_{22} \;\; \sigma_{12} \;\; \sigma_{31} \;\; \sigma_{23}\}^T$ is assumed a vector form of the stress tensor $\boldsymbol{\sigma}$, the stress-strain relation is written in matrix form, as $\{\boldsymbol{\sigma}\}=\boldsymbol{D}\{\boldsymbol{\varepsilon}\}$. $\boldsymbol{D}$ is a matrix of elastic constants. For an isotropic elastic material, it is represented as:

$$\boldsymbol{D} = \frac{E}{(1-\nu^2)} \begin{bmatrix} 1 & \nu & 0 & 0 & 0 \\ \nu & 1 & 0 & 0 & 0 \\ 0 & 0 & \frac{1-\nu}{2} & 0 & 0 \\ 0 & 0 & 0 & \kappa\frac{1-\nu}{2} & 0 \\ 0 & 0 & 0 & 0 & \kappa\frac{1-\nu}{2} \end{bmatrix}. \qquad (5)$$

E and ν are the Young's modulus and the Poisson's ratio, respectively. κ is a shear correction factor and $\kappa=\pi^2/12$ is selected. By employing stress components of $\boldsymbol{\sigma}$, the stress resultants in the flat shell can be written as:

$$\left\{ \begin{array}{c} N_{11} \\ N_{22} \\ N_{12} \end{array} \right\} = \int_{-t/2}^{t/2} \left\{ \begin{array}{c} \sigma_{11} \\ \sigma_{22} \\ \sigma_{12} \end{array} \right\} dx_3,$$

5

$$\left\{ \begin{array}{c} M_{11} \\ M_{22} \\ M_{12} \end{array} \right\} = \int_{-t/2}^{t/2} z \left\{ \begin{array}{c} \sigma_{11} \\ \sigma_{22} \\ \sigma_{12} \end{array} \right\} dx_3,$$

$$\left\{ \begin{array}{c} Q_1 \\ Q_2 \end{array} \right\} = \int_{-t/2}^{t/2} \left\{ \begin{array}{c} \sigma_{31} \\ \sigma_{23} \end{array} \right\} dx_3, \tag{6}$$

where N_{ij}, M_{ij} and Q_i are stress resultants in terms of membrane, bending moment and shear forces, respectively. As for the numerical integration along the shell thickness direction, three-point Newton-Cotes quadrature is adopted.

2.2. Meshfree modeling of cracked folded structure

Meshfree modeling for structural analysis and fracture problems are briefly presented. The detail has been reported and can be found in [46,50,54-56]. RKs are set each node to interpolate deformation of the cracked flat shell as shown in Fig.1(a). The $u_{1mid}(\boldsymbol{x})$, $u_{2mid}(\boldsymbol{x})$, $u_3(\boldsymbol{x})$, $\theta_1(\boldsymbol{x})$ and $\theta_2(\boldsymbol{x})$ in eq.(1) are respectively represented as displacement components in a vector form as $d_i(\boldsymbol{x})$ (i=1, $\cdots$, 5). The approximated vector at position $\boldsymbol{x}$, i.e., $\boldsymbol{d}^h(\boldsymbol{x})=\left\{ d_1^h \ d_2^h \ d_3^h \ d_4^h \ d_5^h \right\}^T$ is written by employing the RKs, as:

$$\boldsymbol{d}^h(\boldsymbol{x}) = \sum_{I=1}^{NP} \Psi_I(\boldsymbol{x})\boldsymbol{d}_I, \tag{7}$$

where $\boldsymbol{d}_I=\{d_{1I} \ d_{2I} \ d_{3I} \ d_{4I} \ d_{5I}\}^T$ is a coefficient vector of the I-th node, and NP is a total number of nodes in the meshfree discretization. $\Psi_I(\boldsymbol{x})$ is a RK in terms of the I-th node. A cubic spline is chosen as the original kernel function $\phi_{aI}(\boldsymbol{x}_I - \boldsymbol{x}, h_I)$, which can be written as:

$$\Psi_I(\boldsymbol{x}) = \boldsymbol{H}^T(\boldsymbol{x}_I - \boldsymbol{x})\boldsymbol{b}(\boldsymbol{x})\phi_{aI}(\boldsymbol{x}_I - \boldsymbol{x}), \tag{8}$$

$$\phi_{aI}(\boldsymbol{x}_I - \boldsymbol{x}, h_I) = \frac{10}{7\pi h_I^2} \left\{ \begin{array}{ll} 1 - \frac{3}{2}s_I^2 + \frac{3}{4}s_I^3 & (0 \le s_I \le 1) \\ \frac{1}{4}(2 - s_I)^3 & (1 \le s_I \le 2) \\ 0 & (2 \le s_I) \end{array} \right. , \tag{9}$$

where s_I ($=||\boldsymbol{x}_I - \boldsymbol{x}||/h_I$) is a normalized distance from center of the kernel. A parameter h_I ($=\alpha_I h_I^p$) is defined for each node. h_I^p is an averaged node

distance surrounding the I-th node, and α_I is a parameter to control the function support. A complete quadratic basis is chosen as the basis vector $\boldsymbol{H}(\boldsymbol{x}) = \{1 \quad x_1 \quad x_2 \quad x_1^2 \quad x_1 x_2 \quad x_2^2\}$ in eq.(8) to satisfy KMRC [34]. This is necessary condition to address the shear locking problem in the plate bending analysis.
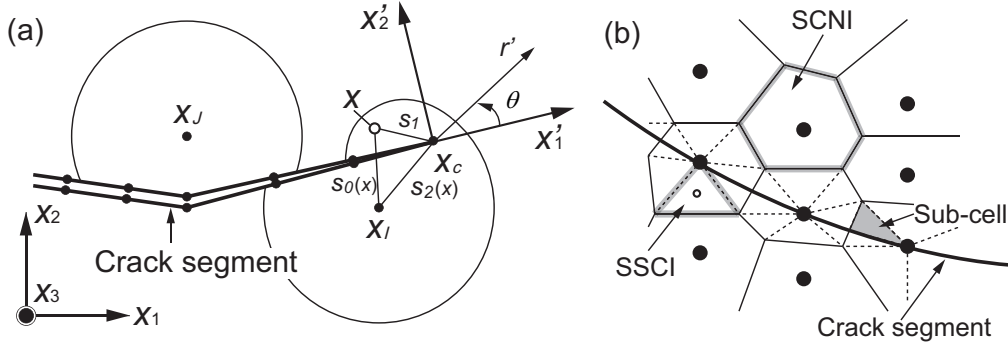

Figure 2: Crack modeling employing the meshfree method. [(a) Diffraction and visibility criterion, (b) SCNI and SSCI for the crack modeling]

A schematic illustration of the meshfree crack modeling is presented in Fig.2(a). The crack segment is represented by assembly of the nodes while double nodes are set along the crack segment. A diffraction method and visibility criterion [52] are introduced. When a crack segment crosses the function support, the function is cut by a visibility criterion. While a diffraction method is adopted when the function support includes the crack tip. The original function support s_I for the I-th node is modified, as:

$$\hat{s}_I = \left(\frac{s_1 + s_2(\boldsymbol{x})}{s_0(\boldsymbol{x})} \right)^\lambda \frac{s_0(\boldsymbol{x})}{h_I}, \tag{10}$$

where $s_0(\boldsymbol{x}) = \|\boldsymbol{x} - \boldsymbol{x}_I\|$, $s_1 = \|\boldsymbol{x}_c - \boldsymbol{x}_I\|$, and $s_2(\boldsymbol{x}) = \|\boldsymbol{x} - \boldsymbol{x}_c\|$ are normalized distances as shown in Fig.2(a), which is evaluated by modifying the original distance s_I in eq.(9). $\boldsymbol{x}_c$ and $\boldsymbol{x}_I$ are position vectors at the crack tip and the I-th node. $\hat{s}_I$ is the modified function support size. A parameter to define the shape of the RKs is set $\lambda = 1.0$. An enriched basis [53] is introduced to effectively represent the $1/\sqrt{r'}$ stress singularity around the crack tip. A sinusoidal function is included in the basis vector as $\boldsymbol{H}(\boldsymbol{x}) = \{1 \quad x_1 \quad x_2 \quad x_1^2 \quad x_1 x_2 \quad x_2^2 \quad \sqrt{r'} \sin(\theta'/2)\}$ where r' and θ' are local polar coordinate originated the crack tip as shown in Fig.2(a). The enriched

7

basis is employed when the crack tip is located within the function support. The discretization of the cracked region is presented in Fig.1(b). The cracked shell is partitioned by the Voronoi cell diagram. A nodal integration technique SCNI [36] and SSCI [38] are adopted for the numerical integration of the stiffness matrix in eq.(2). When the crack segment crosses the Voronoi cell, SSCI is employed by dividing a number of triangular domains while SCNI is adopted for another region.

A drilling DOF is introduced as the six-th DOF in the 5DOFs meshfree flat shell modeling. The virtual work principle including the drilling DOF is presented based on eq.(2), as:

$$\int_{\Omega} \boldsymbol{\sigma} : \delta\boldsymbol{\varepsilon} \; d\Omega + \delta W_T = \delta W, \tag{11}$$

where δW_T is a penalty energy [61] which can be written as:

$$W_T = \kappa_T G t A_K \left[\theta_3 - \frac{1}{2} \left(\frac{\partial u_{2mid}}{\partial x_1} - \frac{\partial u_{1mid}}{\partial x_2} \right) \right]^2, \tag{12}$$

where $G \; (=E/2(1 + \nu))$ is a transverse elasticity modulus and t is a shell thickness. A_K is area of the K-th node Ω_K which is defined by the Voronoi cell. κ_T=0.1 is chosen as a parameter to define the penalty energy. The virtual strain ε_{θ_3} in terms of the drilling DOF θ_3 is defined, as:

$$\varepsilon_{\theta_3} = \theta_3 - \frac{1}{2} \left(\frac{\partial u_{2mid}}{\partial x_1} - \frac{\partial u_{1mid}}{\partial x_2} \right). \tag{13}$$

When a virtual stress R_{θ_3}=$2\kappa_T G \varepsilon_{\theta_3}$ is defined in terms of eq.(13), the penalty energy of eq.(12) can be rewritten as W_T=$R_{\theta_3} \varepsilon_{\theta_3} t A_K / 2$. The virtual strain ε_{θ_3} are integrated by SCNI/SSCI, the detail was given in Ref. [51]. Then, the ε_{θ_3} of the drilling DOF θ_3 can be written, as:

$$\varepsilon_{\theta_3} = \sum_{I=1}^{NP} \left\{ \frac{1}{2} \frac{\partial \Psi_I}{\partial x_2} \quad -\frac{1}{2} \frac{\partial \Psi_I}{\partial x_1} \; 0 \; 0 \; 0 \; \Psi_I \right\} \hat{\boldsymbol{d}}_I$$
$$= \sum_{I=1}^{NP} \boldsymbol{B}_{\theta_3 I} \hat{\boldsymbol{d}}_I, \tag{14}$$

where $\boldsymbol{B}_{\theta_3 I}$ is the displacement-strain relation matrix in terms of the drilling rotation component. $\hat{\boldsymbol{d}}(\boldsymbol{x})$ is the 6DOFs displacement vector. It is rewritten

8

by considering the six-th DOF as well as 5DOFs flat shell, as:

$$\hat{\boldsymbol{d}}^h(\boldsymbol{x}) = \sum_{I=1}^{\mathrm{NP}} \Psi_I(\boldsymbol{x})\hat{\boldsymbol{d}}_I, \qquad (15)$$

where $\hat{\boldsymbol{d}}_I$ is the coefficient vector of the I-th node.
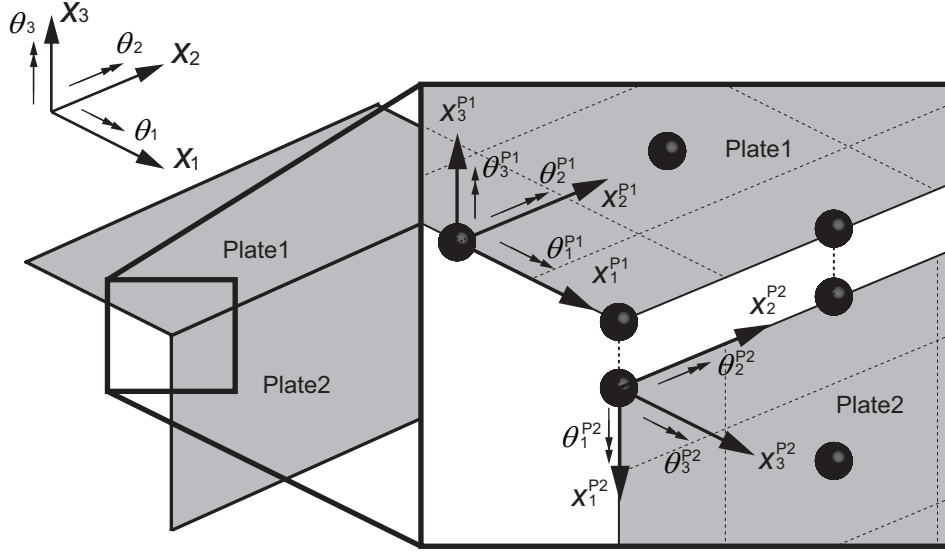

Figure 3: Meshfree modeling for a folded plate structure.

It is well-known that the standard RK does not satisfy so-called Kronecker delta property $\hat{\boldsymbol{d}}^h(\boldsymbol{x}){\neq}\hat{\boldsymbol{d}}_I$. The SK [49] is introduced for essential BC enforcements and modeling of the folded structure. A schematic illustration of the folded structure modeling is presented in Fig.3. There are two plates "Plate 1" "Plate 2" and the local coordinate systems are x_1^{P1}-x_2^{P1}-x_3^{P1} and x_1^{P2}-x_2^{P2}-x_3^{P2}, respectively. A global stiffness matrix of the folded plate structure is generated by employing a transformation matrix [50]. By introducing the 6DOFs flat shell, SK and the transformation matrix, a folded plate structure can be analyzed successfully as well as finite element modeling.

3. Evaluation of the mixed-mode SRIFs

3.1. SRIFs in a cracked flat shell

In the flat shell formulation, plane stress condition is assumed for the membrane deformation while Mindlin-Reissner plate theory is for the bend-

9

ing deformation. When a crack embedded in the flat shell and contact on the crack face is neglected, two membrane and three bending SRIFs can be defined, *i.e.*, crack opening K_{1m} and shear deformation K_{2m} for membrane SIFs and symmetric K_{1b}, anti-symmetric K_{2b} and shear K_{3b} for bending SIFs [58], respectively. A schematic illustration of the deformation modes is represented in Fig.4(a)-(e). It is known that most of the loads are transferred as membrane stresses to the thin walled structure, *e.g.*, the cracked box beam problem, membrane SRIFs K_{1m} and K_{2m} are only treated. For the bending deformation problems, please see [54,56].
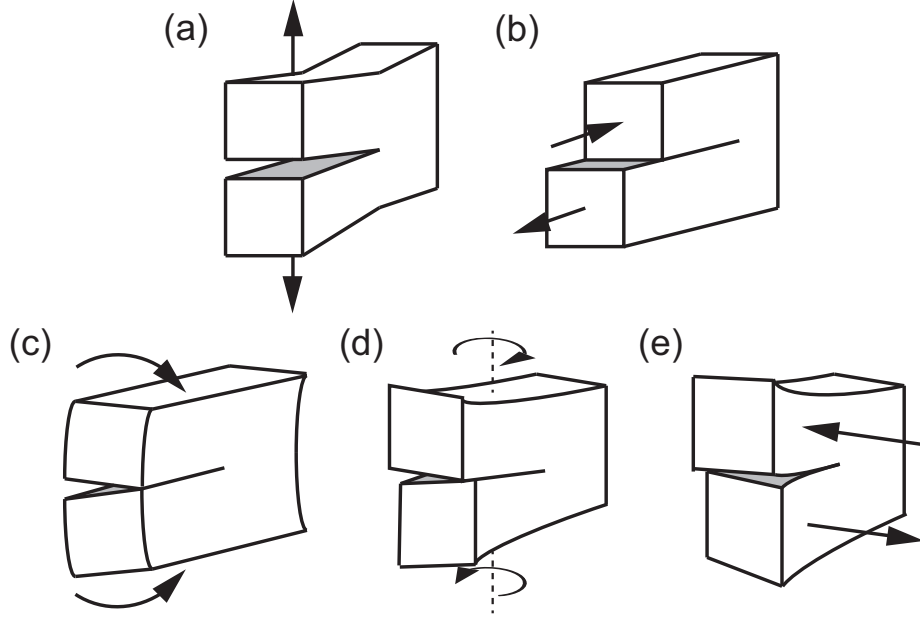
Figure 4: Membrane and moment intensity factors correspond to deformation modes of a cracked body [58]. [(a) K_{1m}, (b) K_{2m}, (c) K_{1b}, (d) K_{2b}, (e) K_{3b}]

3.2. J-integral evaluation for a cracked flat shell

J-integral is employed for analyzing the membrane SRIFs based on the stress resultants of the flat shell. A counter integral form of the J-integral can be written, as:

$$J_{lm} = \int_{\Gamma_{\text{Jint}}} \frac{1}{t} \left(W_m n'_l - N'_{ij} \frac{\partial u'_i}{\partial x'_l} n'_j \right) d\Gamma_{\text{Jint}}, \tag{16}$$

10

where J_{lm} (l=1, 2) are the path-independent integrals with the membrane components in a flat shell. t is a shell thickness. ( )$'$ in eq.(16) is physical values defined by a local coordinate from the crack tip. Γ_{Jint} is an open contour surrounding the crack tip as shown in Fig.5(a). u'_i (i=1,2,3) are displacements along x'_i-axis defined in Fig.5(b). W_m is strain energy density in terms of the membrane deformation. It is written, as:

$$W_m = \int_0^{\varepsilon'} N'_{ij} d\varepsilon'_{ij},$$ (17)

where N'_{ij} is stress resultants defined in eq.(6).
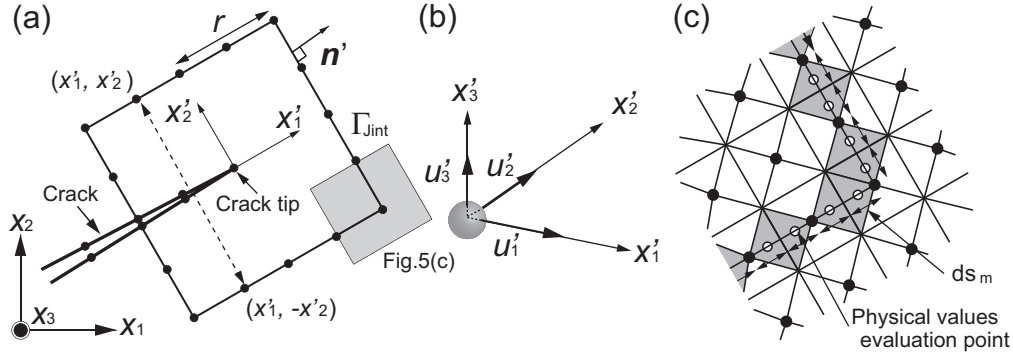
Figure 5: A path-independent integral for membrane deformation. [(a) A contour integral, (b) Displacements based on polar-coordinate system of the crack tip]

The relationship between the J-integral and the SRIFs are represented, as:

$$J_{1m} = \frac{K_{1m}^2 + K_{2m}^2}{\bar{E}},$$ (18)

where $\bar{E}$ is a material parameter. $\bar{E}=E$ is chosen for the assumption of the plane stress condition.

3.3. Mode separation of the J-integral

The J-integral is decomposed into mixed-mode SRIFs K_{1m} and K_{2m} by a decomposition method [55,59,60]. The membrane J-integral component J_{1m} is separated into two modes, as:

$$J_{1m} = J_{1m}^S + J_{1m}^{AS},$$ (19)

11

where J_{1m}^S and J_{1m}^{AS} are separated values of the path-independent integral in terms of the symmetrical and asymmetric deformation across the crack segment. The separated J_{1m}^k can be discretized, as:

$$J_{1m}^k = \int_{\Gamma_{\text{Jint}}} \frac{1}{t} \left(W_m^k n_1' - N_{ij}^k \frac{\partial u_i^k}{\partial x_1'} n_j' \right) d\Gamma_{\text{Jint}}, \tag{20}$$

where $k=S$ and AS. They are symmetric and asymmetric components, respectively. They are evaluated two points (x_1', x_2') and $(x_1', -x_2')$ as shown in Fig.5(a) that located symmetrical position across the crack segment. The separated stress resultants $\boldsymbol{N}^k = \{N_{11}^k \ N_{22}^k \ N_{12}^k\}^T$ $(k=S, AS)$ can be written, as:

$$\boldsymbol{N}^S(x_1', \ x_2') = \frac{1}{2} \left\{ \begin{array}{c} N_{11}'(x_1', \ x_2') + N_{11}'(x_1', \ -x_2') \\ N_{22}'(x_1', \ x_2') + N_{22}'(x_1', \ -x_2') \\ N_{12}'(x_1', \ x_2') - N_{12}'(x_1', \ -x_2') \end{array} \right\}, \tag{21}$$

$$\boldsymbol{N}^{AS}(x_1', \ x_2') = \frac{1}{2} \left\{ \begin{array}{c} N_{11}'(x_1', \ x_2') - N_{11}'(x_1', \ -x_2') \\ N_{22}'(x_1', \ x_2') - N_{22}'(x_1', \ -x_2') \\ N_{12}'(x_1', \ x_2') + N_{12}'(x_1', \ -x_2') \end{array} \right\}. \tag{22}$$

W_m^k in eq.(18) is a strain energy density evaluated by the separated two components. It is written, as:

$$W_m^k = \int_0^{\varepsilon^k} N_{ij}^k d\varepsilon_{ij}^k. \tag{23}$$

The J-integrals in eq.(18) can be transformed into the mixed-mode SRIFs, as:

$$J_{1m}^S = \frac{K_{1m}^2}{\bar{E}}, \qquad J_{1m}^{AS} = \frac{K_{2m}^2}{\bar{E}}. \tag{24}$$

3.4. J-integral discretization employing the meshfree method

A nodal integration technique SSCI is adopted to discretize the separated J-integrals in eq.(20). A schematic illustration of the J-integral discretization is shown in Fig.5(c). A triangular domains are arranged along the contour. The J-integral is discretized by SSCI and physical values along the contour is smoothed. The discretization form can be written, as:

$$\tilde{J}_{1m}^k = \sum_{m=1}^{\text{Ncell}} \frac{1}{t} \left(\tilde{W}_m^k n_1' - \tilde{N}_{ij}^k \frac{\partial \tilde{u}_i^k}{\partial x_1'} n_j' \right)_m ds_m, \quad \tilde{W}_m^k = \frac{1}{2} \tilde{N}_{ij}^k \tilde{\varepsilon}_{ij}^k, \tag{25}$$

where ($\tilde{\ }$) represents smoothed operation for the physical values. Ncell is number of triangular domains along the contour.

4. Numerical examples

In this section, four numerical examples for single- and mixed-mode crack problems are considered to show the accuracy, performance and effectiveness of the developed meshfree approach and the fracture evaluation technique. For the analyses of the cracked flat shell problems, 5DOFs flat shell is adopted while 6DOFs flat shell is chosen for the folded structure problems.

The accuracy of the SRIFs for the numerical and reference solutions is examined. The error η_i % is defined as

$$\eta_i = \frac{|K_i^{\text{Num.}} - K_i^{\text{Ref.}}|}{K_i^{\text{Ref.}}} \times 100 \ \ [\%], \tag{26}$$

where $K_i^{\text{Num.}}$ and $K_i^{\text{Ref.}}$ (i=1m, 2m) are the numerical and reference solutions, respectively.

4.1. A flat shell including a center crack under tensile load

A rectangular flat shell including a center through crack under tensile load is analyzed. The geometry is shown in Fig.6(a). The width is b=10 mm and the height c=2b. The crack length is varied from a/b=0.1 to 0.7. Two kinds of shell thickness t are chosen, *i.e.*, b/t=2 and 10, respectively. E=210 GPa and ν=0.3 are chosen for the material property.

A close-up view of the meshfree model for a/b=0.5 is presented in Fig.6(b). Half of the structure x_1>0 (shaded region in Fig.6(a)) is modeled. The nodes are uniformly distributed to an entire model. The support size is set to α_I=2.5. Voronoi cell diagram is applied to an entire model to generate the meshfree model. The cell is sub-divided around the segment for the crack modeling and the J-integral evaluation. When imposing the essential BCs, u_3=0 along x_2=-c and x_2=c; u_{1mid}=u_{2mid}=0 on x_1=b, x_2=-c; u_{1mid}=0 on x_1=b, x_2=c, respectively. For assuming symmetrical BCs, u_{1mid}=θ_2=0 along x_1=0. Uniform tensile pressure p_0 is applied along the edges x_2=$\pm c$. The mode-I SRIF K_{1m} is normalized, as: $F_{1m}(=K_{1m}/\frac{p_0}{t}\sqrt{\pi a})$ where F_{1m} is normalized mode-I SRIF.

A path independency of the mode-I SRIF is firstly examined. A rectangular contour is adopted for the J-integral evaluation as shown in Fig.6(b).
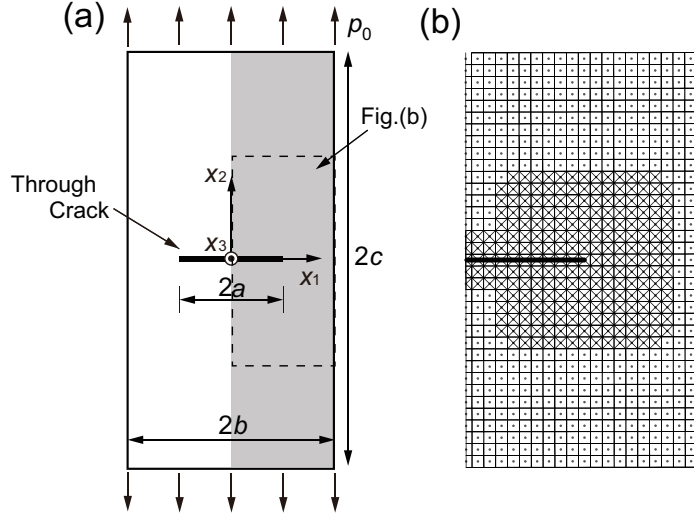
13

Figure 6: A rectangular flat shell including a center crack. [(a) Analysis model to be solved, (b) A close-up view of the meshfree model for $a/b=0.5$]

The results for the case of $a/b=0.5$ are presented in Fig.7(a) for $b/t=2$ and 10. r is a parameter to define size of the contours. The vertical axis is the normalized SRIF and the horizontal axis is parameter r. As the reference solution, a rectangular domain including a centered crack [63] is adopted. The reference solution is for $2b/c=\infty$. A path independency of the SRIF can be found for $b/t=2$ and 10. In addition, the SRIF is evaluated by changing the crack length a/b and they are compared with the reference solutions. The results are shown in Fig.6(b) from $a/b=0.1$ to 0.7, respectively. Same normalized SRIF are obtained for $b/t=2$ and 10, and they are good agreement with the reference solutions. It is found that the normalized mode-I SRIF in flat shell under uniform load coincides with the mode-I SIF in 2D problems.

4.2. A cruciform test specimen including a center crack under tensile load

A cruciform test specimen including an inclined through crack is analyzed. The model subjected to tensile load is represented in Fig.8(a). The specimen is modeled by the flat shell with a thickness t of 1.0 mm. Whole model is discretized. The size is $b_1=165$ mm, $b_2=100$ mm, $c_1=75$ mm, and $c_2=50$ mm. The half crack length a is varied, including $a/c_2=0.4$, 0.6, 0.8 and 1.0, respectively. $E=200$ GPa and $\nu=0.3$ are chosen. Fig.8(b) is a close-up
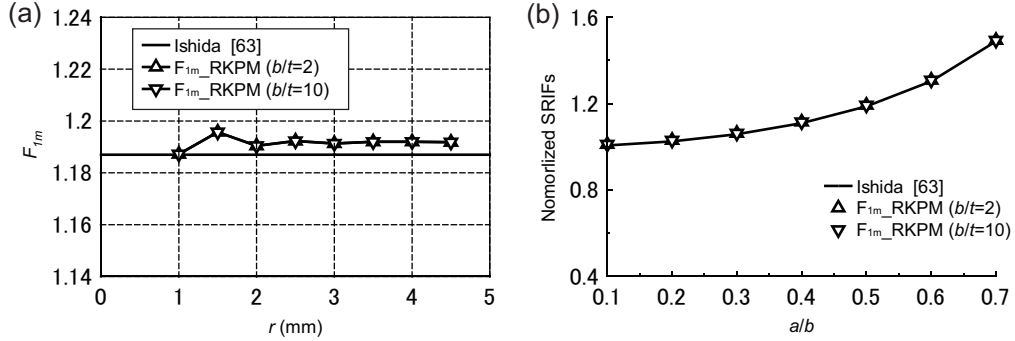
Figure 7: Normalized SRIFs for various path radius when $b/t=2$ and 10. [(a) Path independency, (b) Variations of the SRIF for a/b]

view of the meshfree model when $a/c_2=0.6$ and $\omega=\pi/4$ deg.. The support size is set from $\alpha_I=2.6$ to 2.7. As the essential BCs, $u_{1mid}=u_3=\theta_1=\theta_2=0$ on $x_1=c_1$, $x_2=-b_1$; $u_{1mid}=0$ on $x_1=c_1$, $x_2=b_1$, respectively. To suppress the rigid rotation, $u_{2mid}=0$ on $x_1=0$, $x_2=0$ is applied to one side of the crack segment. Uniform pressure p_0 is applied along $x_2=\pm b_1$. The normalized SRIFs $F_{1m}(=K_{1m}/\frac{p_0}{t}\sqrt{\pi a})$ and $F_{2m}(=K_{2m}/\frac{p_0}{t}\sqrt{\pi a})$ are evaluated.
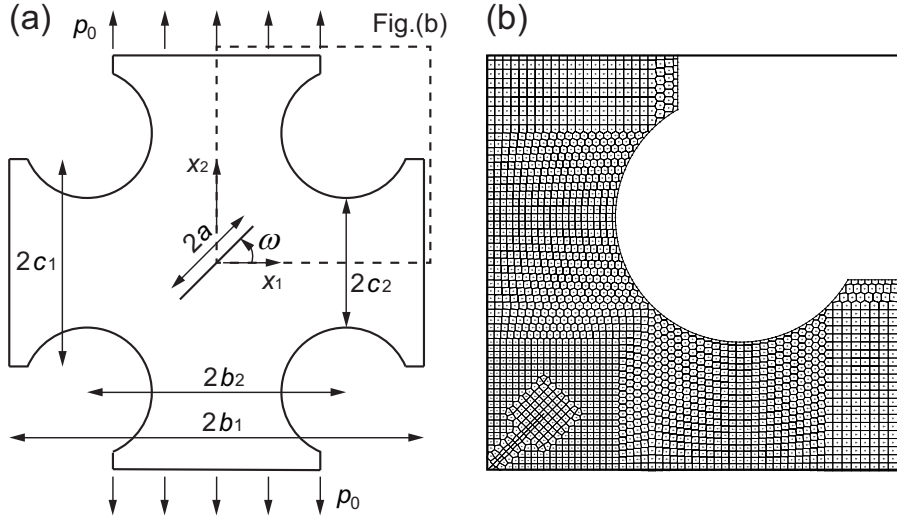
Figure 8: A cruciform test specimen including an inclined center crack. [(a) Analysis model to be solved, (b) Close-up view of the meshfree model for $a/c_2=0.6$ and $\omega=\pi/4$ deg.]

Path independency of the mixed-mode SRIFs is examined for $a/c_2=0.8$,

15

$\omega = \pi/4$ deg.. The results are presented in Fig.9(a) and (b) for F_{1m} and F_{2m}, respectively. As the reference solutions, mixed-mode SIFs for 2D problems evaluated by FEM [64] are adopted. It is found that the mixed-mode SRIFs are path independency. The SRIFs are compared with the reference solutions by changing the crack length, $a/c_2 = 0.6$, 0.8 and 1.0 for the inclined angle from 0 to $\pi/2$ deg.. The results are also good agreement with the 2D SIFs. It is confirmed that the SRIFs in a flat shell can be evaluated in high accuracy for the meshfree modeling under tensile load.
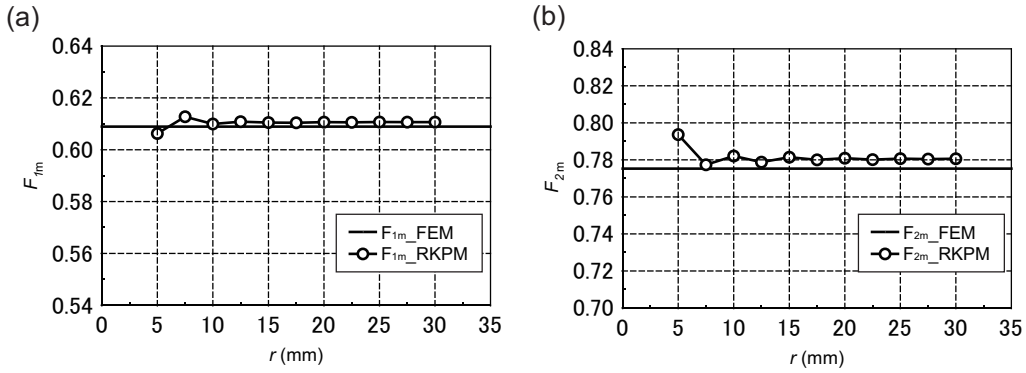
Figure 9: Normalized mixed-mode SRIFs for various path radius when $a/c_2 = 0.8$ and $\omega = \pi/4$ deg.. [(a) F_{1m}, (b) F_{2m}]
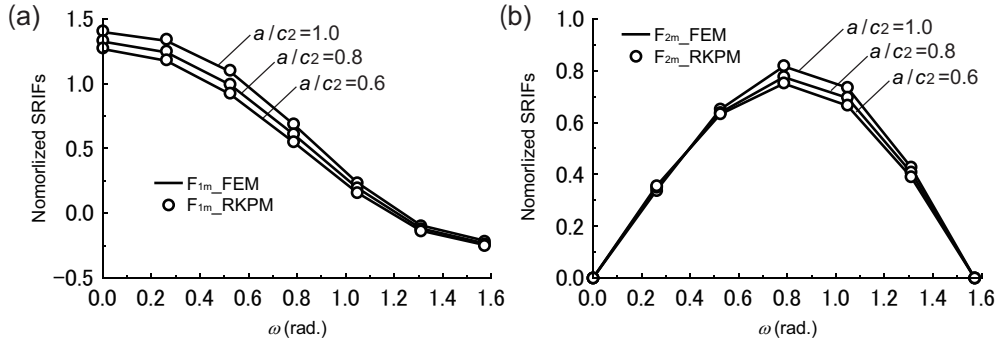

Figure 10: Normalized mixed-mode SRIFs for various crack angle when $a/c_2 = 0.6$, 0.8 and 1.0. [(a) F_{1m}, (b) F_{2m}]

4.3. A stiffened plate with an edge crack under tensile load

A stiffened plate including an inclined through crack under tensile load shown in Fig.11(a) is considered. The length of plate-1 and plate-2 is $L_1 = 60$

16

mm. The width of plate-2 is L_2=30 mm and the height of plate-1 is L_3=30 mm. The thickness of both plates is t=0.3 mm. The crack length a is set to 5, 10, 15 and 20 mm, respectively, which is located at plate-1 and crack angle ω=0, 30 and 45 deg.. The meshfree model for a=10 mm and ω=30 deg. is presented in Fig.11(b) and the close-up view of plate-1 is shown in Fig.11(c). The support size is set from α_I=2.5 to 2.7. E=200 GPa and ν=0.3 are chosen. In stiffened plate model, $u_{1mid}=u_{2mid}=u_3$=0 on $x_1=L_1/2$, $x_2=x_3$=0; u_{1mid}=0 on $x_1=L_1/2$, $x_2=L_2$, $x_3=L_3$; u_3=0 on x_1=0 and L_1, $x_2=L_2$, x_3=0 and only uniform pressure p_0 is applied along both edges of plate-1 on x_2=0 and 60 mm, as shown in Fig.11(a). The normalized SRIFs $F_{1m}(=K_{1m}/\frac{p_0}{t}\sqrt{\pi a})$ and $F_{2m}(=K_{2m}/\frac{p_0}{t}\sqrt{\pi a})$ are evaluated.
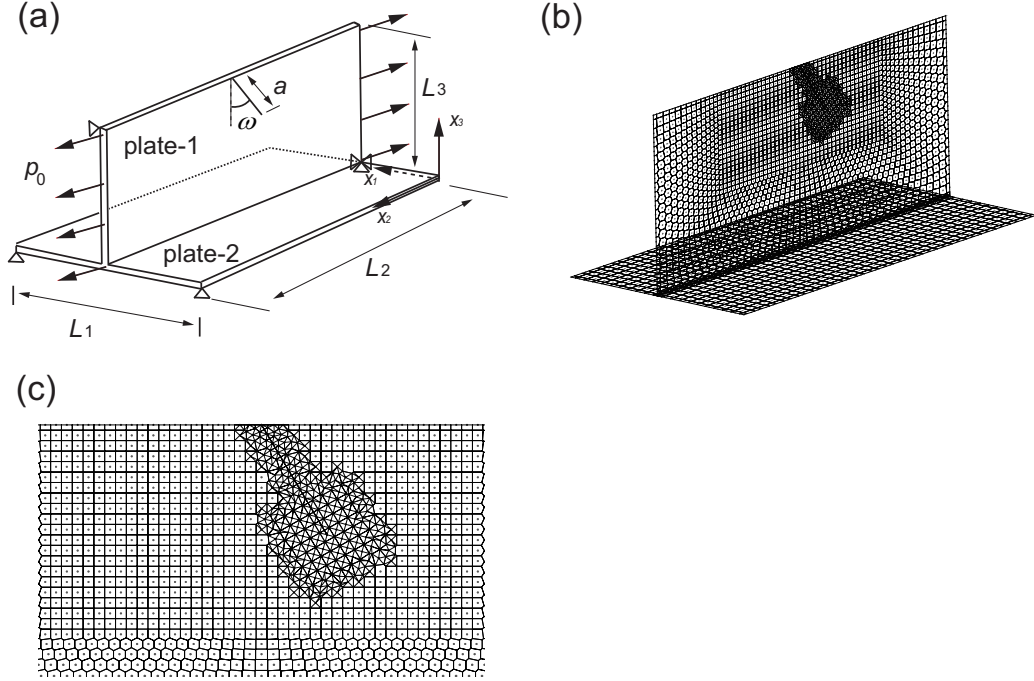

Figure 11: A stiffened plate including an inclined edge crack. [(a) Analysis model to be solved, (b) Meshfree model for a=10 mm and ω=30 deg., (c) Close-up view of meshfree model on plate-1 for a=10 mm and ω=30 deg.]

Path independency of the mixed-mode SRIFs is examined for a=10 mm and ω=30 deg.. The results are presented in Fig.13(a) and (b) for F_{1m} and F_{2m}, respectively. The results of path independency are compared with commercial FEM software, Abaqus [65]. It provides an evaluation of the
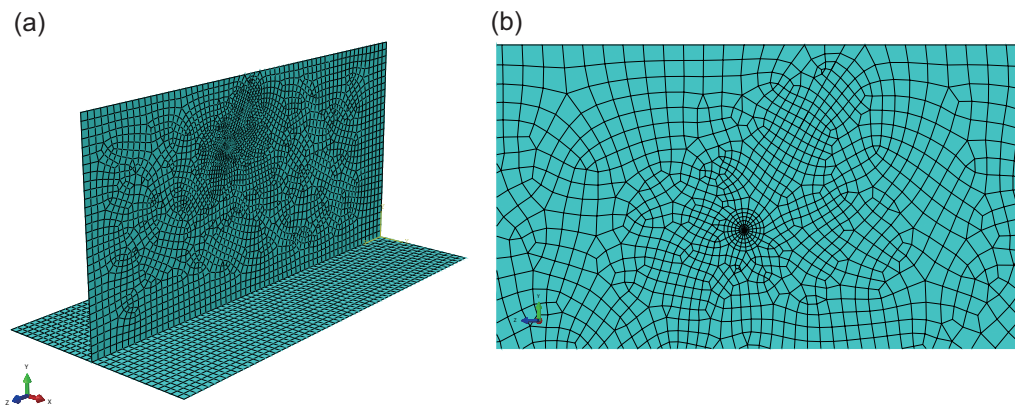
Figure 12: FEM model for cracked stiffened plate for a=10 mm and ω=30 deg.. [(a) FEM model, (b) Close-up view]

J-integral and an interaction integral method to extract individual SIFs for a crack under mixed-mode loading. For the FEM model in Fig.4.3, the crack tip is surrounded by 3-node triangular S3 shell elements; the remaining area is meshed by 4-node quadrilateral S4R shell elements. The element size is 0.2 mm near the crack tip; the element size is 0.4-0.5 mm along crack in the FEM model to get fully converged solution. The FEM results are average of SIFs for five contours. It is found that the mixed-mode SRIFs are path independency. The SRIF is calculated by changing crack length for different crack angles and they are compared with the FEM results. The results are shown in Fig.14. The SRIFs have good accuracy of proposed method for different crack length and crack angle. It indicates that the meshfree method can be an effective approach for stiffened plate with crack.

Table 1: Comparison for SRIFs of stiffened plate (ω=0 deg.)

ω=0 deg.			
	RKPM	FEM	
a	F_{1m}	F_{1m}	η_{1m}
5	1.529	1.524	0.33%
10	1.855	1.848	0.41%
15	2.566	2.550	0.59%
20	4.278	4.239	0.93%

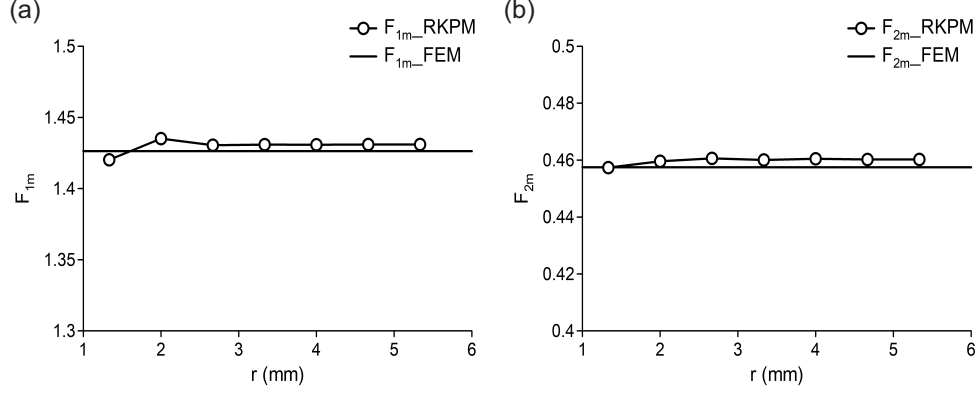The influence of stiffener (plate-2) on plate-1 is discussed in this presented

Figure 13: Normalized mixed-mode SRIFs for various path radius when a=10 mm and ω=30 deg.. [(a) F_{1m}, (b) F_{2m}]

Table 2: Comparison for SRIFs of stiffened plate (ω=30 deg.)

ω=30 deg.						
	RKPM		FEM			
a	F_{1m}	F_{2m}	F_{1m}	F_{2m}	η_{1m}	η_{2m}
5	1.233	0.410	1.231	0.406	0.19%	0.88%
10	1.430	0.461	1.426	0.458	0.28%	0.68%
15	1.858	0.546	1.849	0.542	0.49%	0.82%
20	2.711	0.693	2.691	0.693	0.72%	0.03%

Table 3: Comparison for SRIFs of stiffened plate (ω=45 deg.)

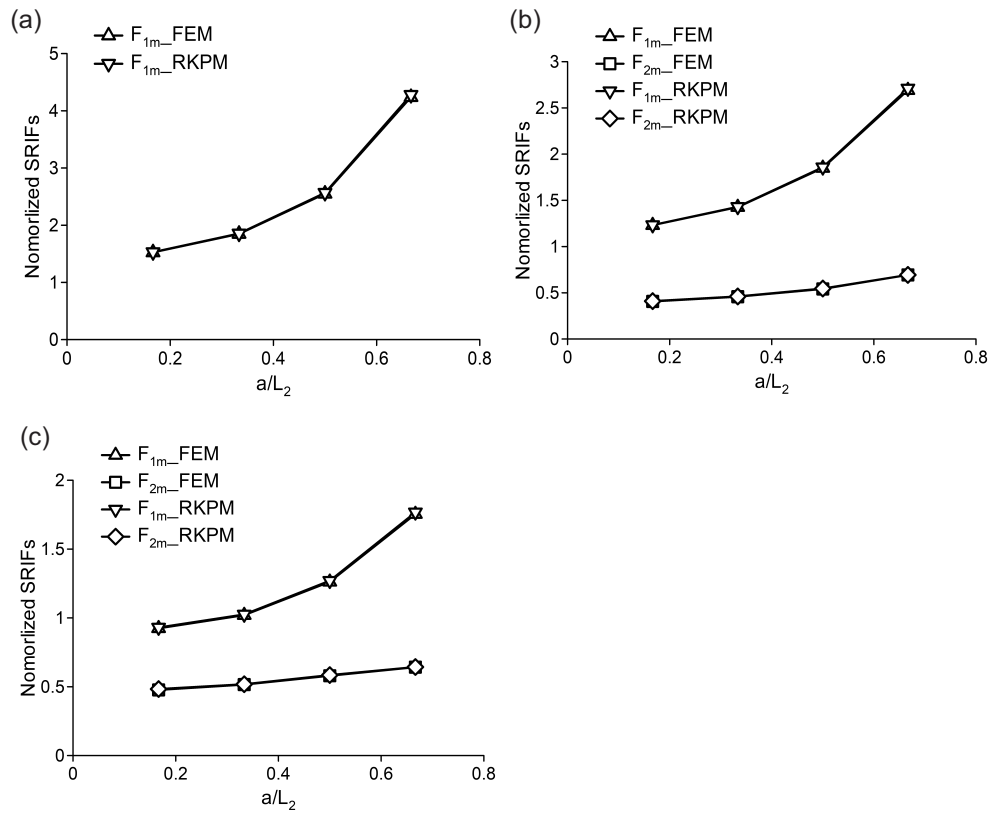| ω=45 deg.						
	RKPM		FEM			
a	F_{1m}	F_{2m}	F_{1m}	F_{2m}	η_{1m}	η_{2m}
5	0.930	0.483	0.924	0.477	0.66%	1.34%
10	1.025	0.518	1.020	0.516	0.51%	0.46%
15	1.270	0.585	1.262	0.580	0.66%	0.80%
20	1.767	0.643	1.754	0.642	0.77%	0.13%

19

Figure 14: Normalized mixed-mode SRIFs for various crack angles when a=5, 10, 15 and 20 mm. [(a) 0 deg., (b) 30 deg., (c) 45 deg.]

paper. Two different Young's moduli E for the stiffener, *e.g.*, E=200 GPa and e=E/100 GPa, are particularly investigated. Fig.15 shows the normalized SRIFs of different Young's modulus for stiffener for various cases. The computed results are also compared with reference solution of 2D rectangular plate for which E=0 GPa for the stiffener is taken. Here, EE and Ee stand for the Young's moduli for plate-1 and plate-2, respectively. It is found that the SRIF results of Ee and 2D plate are very close. Two different phenomena in each figure could be observed. When a/L_2 is lower than critical value, the SRIFs of EE are larger than that of Ee and 2D plate. On the contrary, the SRIFs of EE are smaller than SRIFs of Ee and 2D plate when a/L_2 is higher than critical value. The critical values are 0.37, 0.42 and 0.51 when crack angle is 0, 30 and 45 deg., respectively. The a_ω in Fig.15(d) can be obtained from crack length times cosine of crack angle. It is found that all of a_ω approximately equal 10-11 mm (about one-third of plate width). It means that the stiffener can significantly reduce the values of the SRIF when the crack length of perpendicular direction a_ω gets over one-third of plate width.

4.4. A box beam with a through crack under bending and torsion load

The last numerical example deals with a cracked cantilever box beam under bending and torsion load. The geometry and BC are sketched in Fig.16. The size of the box beam is L_1=800 mm, L_2=800 mm and L_3=100 mm. Four flat shells are joined each other to form the box beam structure. The shell thickness is t=2.0 mm. The material property is E=70 GPa and ν=0.3. The half crack length a is varied and SRIFs are investigated. As the essential BCs., one side of the box beam on x_2=0 mm is clamped. As the load conditions, force couple f=5,000 N is applied on x_2=L_2, x_3=0 as shown in Fig.16. Half meshfree model and close-up view of top plate are represented in Fig.17(a) and (b) for a=200 mm. The symmetry and anti-symmetry BCs are applied along x_1=200 mm for bending case and torsion case, respectively. The symmetry is set to u_{1mid}=θ_2=0; the anti-symmetry is set to u_{2mid}=u_3=θ_1=0. The support size is α_I=2.5 to 2.7 in meshfree model. The normalized SRIFs of bending and torsion are respectively represented, as:

$$F_{1m} = K_{1m}/(\sigma_{\max}\sqrt{\pi a}); F_{2m} = K_{2m}/(\sigma_{\max}\sqrt{\pi a}), \qquad (27)$$

$$F_{1m} = K_{1m}/(\tau_{\max}\sqrt{\pi a}); F_{2m} = K_{2m}/(\tau_{\max}\sqrt{\pi a}), \qquad (28)$$
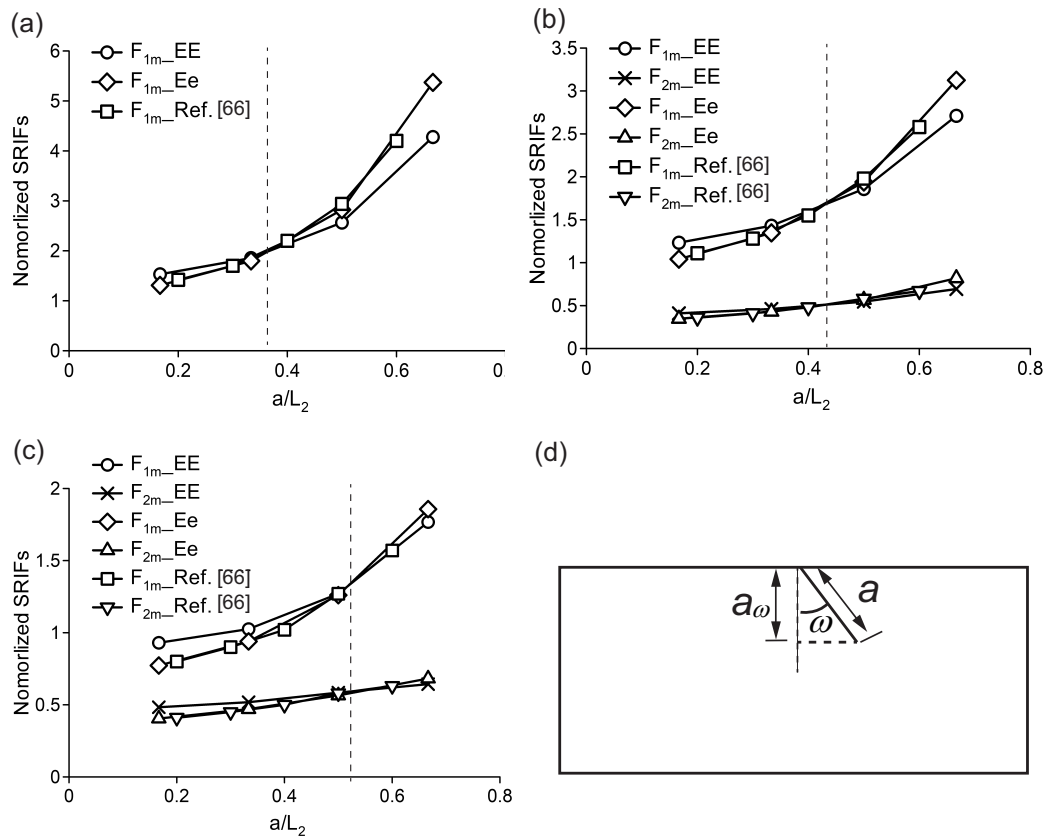
21

Figure 15: Normalized mixed-mode SRIFs for various Young's modulus of stiffener. [(a) 0 deg., (b) 30 deg., (c) 45 deg., (b) Schematic diagram of a_ω on stiffened plate]

where $\sigma_{\max}$ and $\tau_{\max}$ are the maximum stress of bending and torsion, as:

$$\sigma_{\max} = 2f(L_2)(L_3/2)/\bar{I}, \tag{29}$$

$$\tau_{\max} = \frac{2f}{\bar{I}}\left[\frac{L_3 - 2t}{4} + \frac{L_1}{2}(L_3 - t)\right]. \tag{30}$$

$\bar{I}$ is the moment of inertia, as:

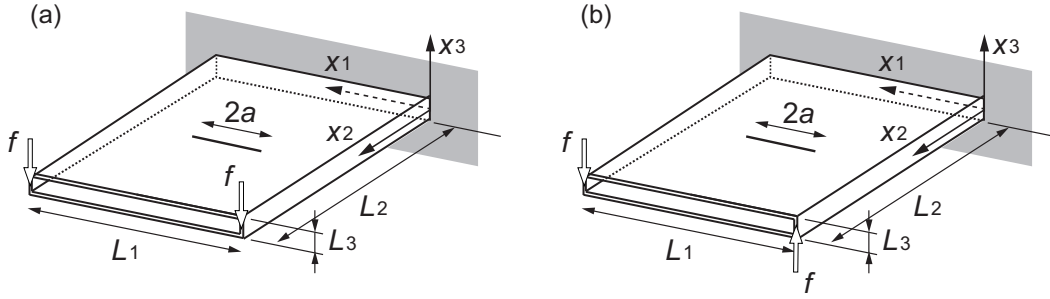$$\bar{I} = \frac{1}{12}\left[L_1 L_3^3 - (L_1 - 2t)(L_3 - 2t)^3\right]. \tag{31}$$

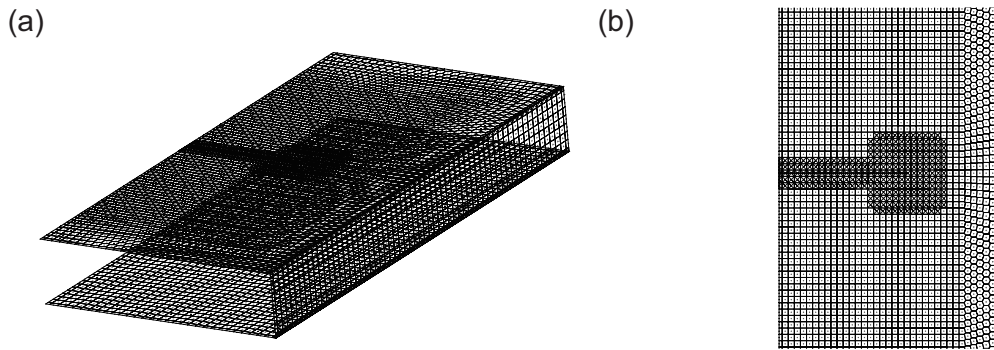Figure 16: A cantilever box beam including a through crack. [(a) Bending, (b) Torsion]

Figure 17: Meshfree model of cracked box beam. [(a) Meshfree model for a=200 mm, (b) Close-up view of top plate for a=200 mm]
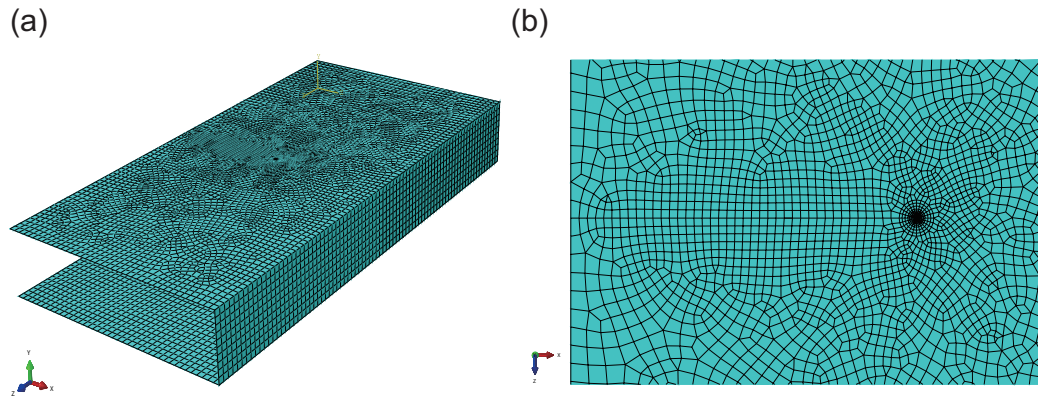
Figure 18: FEM model of cracked box beam for a=200 mm. [(a) Whole view , (b) Close-up view of top plate
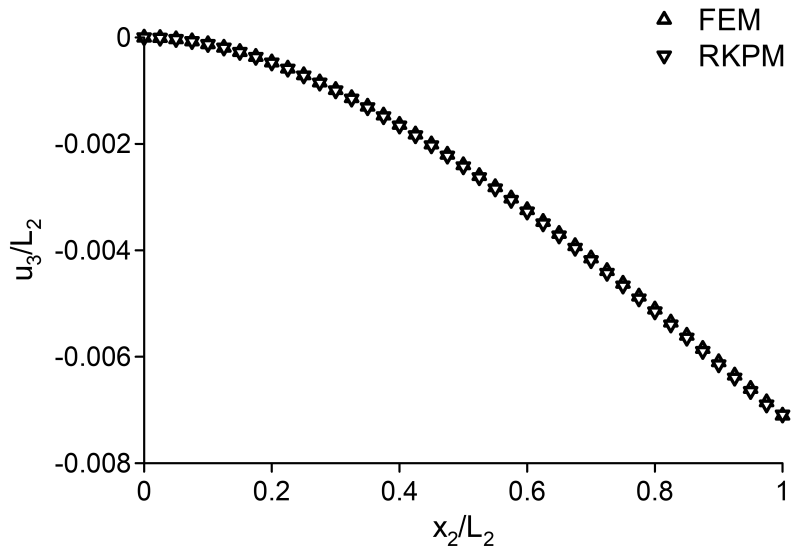

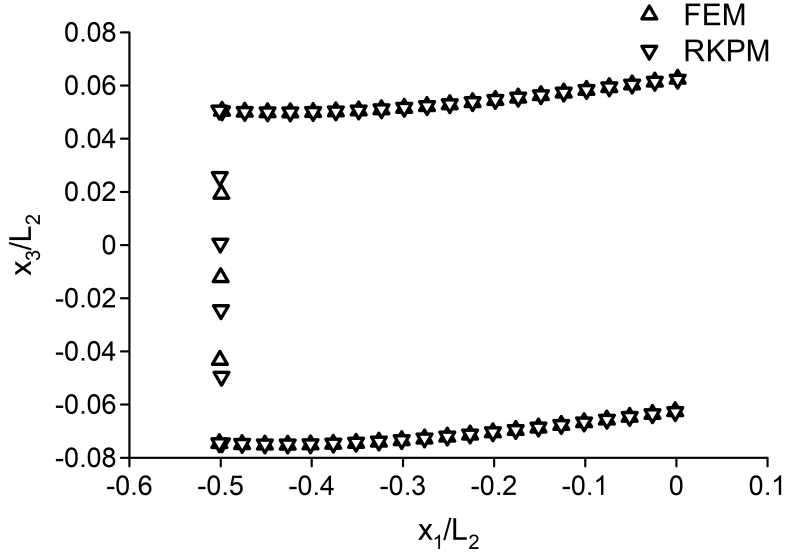Figure 19: Deformed shape of the box beam due to bending.

Figure 20: Deformed shape of the box beam due to torsion.

Prior to cracked box beam, the box beam model without crack is firstly analyzed. Fig.19 shows u_3 deflection results along the center line on the top plate between RKPM and FEM due to bending. Fig.20 visualizes the deformed shape on x_2=800 mm between RKPM and FEM due to torsion. The RKPM results have good agreement with FEM solutions on both cases.

Fig.21(a)-(d) show normalized SRIFs for a=200 mm with different contours for J-integral on bending and torsion loads. As same as the third example, the 3-node triangular S3 shell elements and 4-node quadrilateral S4R shell elements are used in model, as shown in Fig.4.4. The element size is 1.0 mm near the crack tip; the element size is 2.0-7.5 mm along crack to obtain fully converged results. The FEM result are average of stress intensity factors for five path contours. The path-independency of the mixed-mode SRIFs is examined. The normalized SRIFs for both mode-I and mode-II considering various crack lengths are plotted in Fig.22. The SRIFs results are compared with the FEM results. For different crack lengths, the SRIFs which are calculated by the developed method are in good agreement with the FEM solutions. It is confirmed that cracked box beam, such kind of folded structures, can be successfully simulated by the proposed meshfree
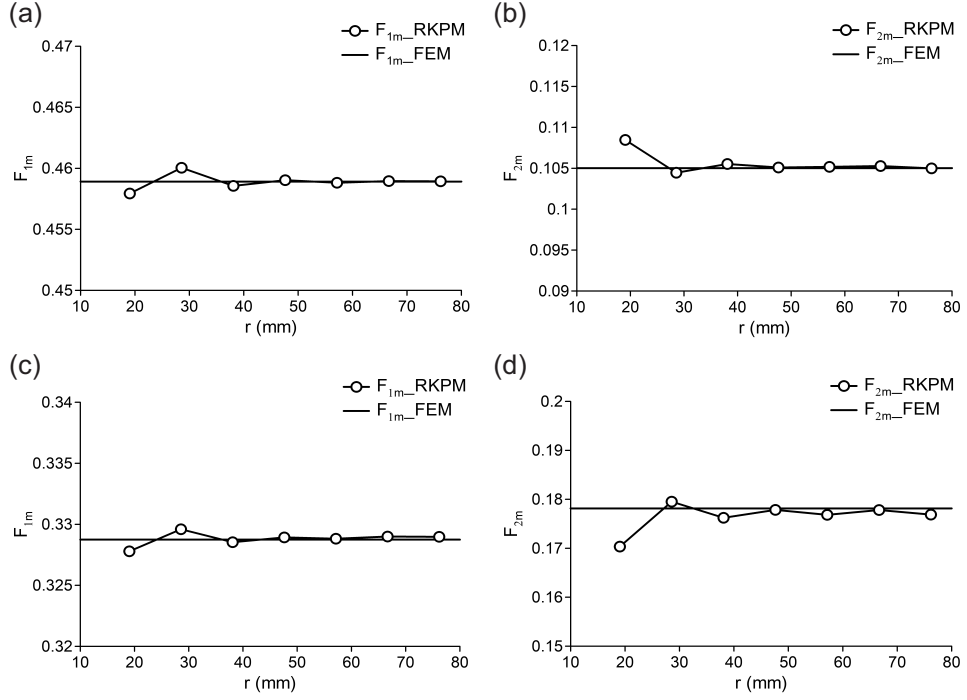
25

modeling.

Figure 21: Normalized mixed-mode SRIFs for various path radius when a=200 mm. [(a) F_{1m} under bending, (b) F_{2m} under bending, (c) F_{1m} under torsion, (d) F_{2m} under torsion]

Table 4: Comparison for SRIFs of box beam (Bending).

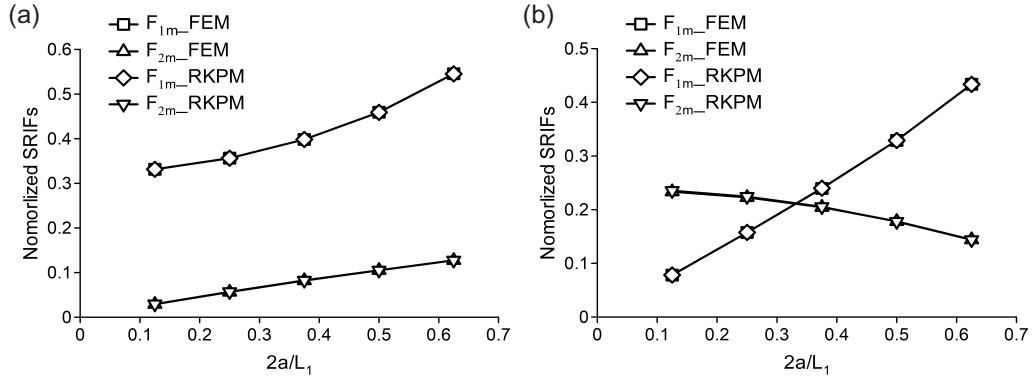| Bending						
	RKPM		FEM			
$2a$	F_{1m}	F_{2m}	F_{1m}	F_{2m}	η_{1m}	η_{2m}
100	0.332	0.029	0.331	0.029	0.20%	0.13%
200	0.357	0.056	0.356	0.056	0.08%	0.01%
300	0.399	0.082	0.398	0.082	0.21%	0.30%
400	0.459	0.105	0.459	0.105	0.05%	0.03%
500	0.545	0.127	0.546	0.127	0.05%	0.12%

Figure 22: Normalized mixed-mode SRIFs for various crack lengths. [(a) Bending, (b) Torsion]

Table 5: Comparison for SRIFs of box beam (Torsion).

Torsion						
	RKPM		FEM			
$2a$	F_{1m}	F_{2m}	F_{1m}	F_{2m}	η_{1m}	η_{2m}
100	0.078	0.234	0.078	0.234	0.24%	0.03%
200	0.157	0.223	0.157	0.223	0.00%	0.07%
300	0.240	0.204	0.240	0.204	0.07%	0.42%
400	0.329	0.178	0.329	0.178	0.02%	0.26%
500	0.433	0.144	0.434	0.144	0.05%	0.26%

5. Conclusion

The effective meshfree Galerkin formulation is presented for single-mode and mixed-mode fracture problems. To simulate the behavior of folded structures, an enhanced 6DOFs flat shell model has been developed by integrating a drilling DOF into the existing 5DOFs meshfree flat shell model. In addition, the numerical integration technique is based on SCNI and SSCI for not only virtual work principle but also J-integral. The decomposition procedure is applied to separate mixed-mode SRIFs into mode-I and -II SRIFs. Several numerical examples are investigated, including flat shell, stiffened plate and box beam. The SRIFs are calculated and the path-independency of SRIFs are examined. The SRIFs of proposed method are compared with reference solutions and FEM solutions. The comparison reveals that high accuracy on SRIFs from meshfree modeling are obtained. In addition, it should be note that the stiffener can significantly decrease the values of SRIF when the crack length of perpendicular direction over one-third of plate width. From several numerical examples, it indicates that the presented formulation can be a effectively approach in modeling crack problems of folded structure.

Acknowledgements

References

[1] D.O. Potyondy, P.A. Wawrzynek, A.R. Ingraffea, Discrete crack growth analysis methodology for through cracks in pressurized fuselage structures, Int. J. Numer. Meth. Eng. 38 (1995) 1611-1633.

[2] L.S. Etube, Fatigue and fracture mechanics of offshore structures, Professional Engineering Publishing Limited, Bury St Edmunds, 2001.

[3] T. Dirgantara, M.H. Aliabadi, Numerical simulation of fatigue crack growth in pressurized shells, Int. J. Fatigue 24 (2002) 725-738.

[4] M. Toyosada, K. Gotoh, T. Niwa, Fatigue life assessment for welded structures without initial defects: an algorithm for predicting fatigue crack growth from a sound site, Int. J. Fatigue 26 (2004) 993-1002.

[5] A. Ahmed, X. Qian, A toughness based deformation limit for fatigue-cracked X-joints under in-plane bending, Mar. Struct. 42 (2015) 33-52.

[6] S.T. Lie, T. Li, Y.B. Shao, S.P. Vipin, Plastic collapse load prediction of cracked circular hollow section gap K-joints under in-plane bending, Mar. Struct. 50 (2016) 20-34.

[7] S.N. Atluri, Computational Methods in the mechanics of fracture, Elsevier Science Publishers, Amsterdam, 1986.

[8] T.L. Anderson, Fracture mechanics: Fundamentals and applications, CRC Press, Boca Raton, 2005.

[9] G.C. Sih, Plates and shells with cracks: Mechanics of fracture Vol.3, Noordhoff International Publishing, Dordrecht, 1977.

[10] H.A. Sosa, J.W. Eischen, Computation of stress intensity factors for plate bending via a path-independent integral, Eng. Fract. Mech. 25 (1986) 451-462.

[11] H.A. Sosa, G. Herrmann, On invariant integrals in the analysis of cracked plates, Int. J. Fract. 40 (1989) 111-126.

[12] J. Dolbow, N. Moës, T. Belytschko, Modeling fracture in Mindlin-Reissner plates with the extended finite element method, Int. J. Solid. Struct. 37 (2000) 7161-7183.

[13] T. Belytschko, T. Black, Elastic crack growth in finite elements with minimal remeshing, Int. J. Numer. Meth. Eng. 45 (1999) 601-620.

[14] N. Moës, J. Dolbow, T. Belytschko, A finite element method for crack growth without remeshing, Int. J. Numer. Meth. Eng. 46 (1999) 131-150.

[15] P.M. Baiz, S. Natarajan, S. Bordas, P. Kerfriden, T. Rabczuk, Linear buckling analysis of cracked plates by SFEM and XFEM, J. Mech. Mater. Struct. 6 (9-10), 1213-1238.

[16] S. Natarajan, P.M. Baiz, M. Ganapathi, P. Kerfriden, S. Bordas, Linear free flexural vibration of cracked functionally graded plates in thermal environment, Comput. Struct. 89 (15-16), 1535-1546.

[17] S. Natarajan, P.M. Baiz, S. Bordas, T. Rabczuk, P. Kerfriden, Natural frequencies of cracked functionally graded material plates by the extended finite element method, Compos. Struct. 93 (11), 3082-3092.

[18] T. Dirgantara, M.H. Aliabadi, Dual boundary element formulation for fracture mechanics analysis of shear deformable shells, Int. J. Solid. Struct. 38 (2001) 7769-7800.

[19] M.H. Aliabadi, A new generation of boundary element methods in fracture mechanics, Int. J. Fract. 86 (1997) 91-125.

[20] T. Belytschko, Y.Y. Lu, L. Gu, Element-free Galerkin Methods, Int. J. Numer. Meth. Eng. 37 (1994) 229-256.

[21] W.K. Liu, S. Jun, Y.F. Zhang, Reproducing kernel particle methods, Int. J. Numer. Meth. Fluid. 20 (1995) 1081-1106.

[22] S.N. Atluri, T. Zhu, A new meshless local Petrov-Galerkin (MLPG) approach in computational mechanics, Comput. Mech. 22 (1998) 117-127.

[23] T.J.R. Hughes, J.A. Cottrell, Y. Bazilevs, Isogeometric analysis: CAD, finite elements, NURBS, exact geometry and mesh refinement, Comput. Meth. Appl. Mech. Engrg. 194 (2005) 4135-4195.

[24] S. Tanaka, H. Okada, S. Okazawa, A wavelet Galerkin method employing B-spline bases for solid mechanics problems without the use of a fictitious domain, Comput. Mech. 50 (2012) 35-48.

[25] S. Tanaka, H. Okada, S. Okazawa, M. Fujikubo, Two-dimensional fracture mechanics analyses using the wavelet Galerkin method and extended finite element method, Int. J. Numer. Meth. Eng. 93 (2013) 1082-1108

[26] S. Tanaka, H. Suzuki, S. Ueda, S. Sannomaru, An extended wavelet Galerkin method with a high-order B-spline for 2D crack problems, Acta Mech. 226 (2015) 2159-2175.

[27] S. Tanaka, S. Sannomaru, M. Imachi, S. Hagihara, S. Okazawa, H. Okada, Analysis of dynamic stress concentration problems employing spline-based wavelet Galerkin method, Eng. Anal. Bound. Elem. 58 (2015) 129-39.

[28] S. Sannomaru, S. Tanaka, K. Yoshida, T.Q. Bui, S. Okazawa, S. Hagihara, Treatment of Dirichlet-type boundary conditions in the spline-based wavelet Galerkin method employing multiple point constraints, Appl. Math. Model. 43 (2017) 592-610.

[29] H. Noguchi, T. Kawashima, T. Miyamura, Element free analyses of shell and spatial structures, Int. J. Numer. Meth. Eng. 47 (2000) 1215-1240.

[30] L. Zhang, J. Wang, Y.H. Zhou, Wavelet solution for large deflection bending problems of thin rectangular plates, Arch. Appl. Mech. 85 (2015) 355-365.

[31] T. Yu, T.Q. Bui, S. Yin, D.H. Doan, C.T. Wu, T. Van Do, S. Tanaka, On the thermal buckling analysis of functionally graded plates with internal defects using extended isogeometric analysis, Compos. Struct. 136 (2016) 684-695.

[32] T. Yu, S. Yin, T.Q. Bui, S. Xia, S. Tanaka, S. Hirose, NURBS-based isogeometric analysis of buckling and free vibration problems for laminated composites plates with complicated cutouts using a new simple FSDT theory and level set method, Thin-Walled Struct. 101 (2016) 141-156.

[33] S. Sadamoto, M. Ozdemir, S. Tanaka, K. Taniguchi, T.T. Yu, T.Q. Bui, An effective meshfree reproducing kernel method for buckling analysis of cylindrical shells with and without cutouts, Comput. Mech. 59 (2017) 919-932.

[34] D. Wang, J.S. Chen, Locking-free stabilized conforming nodal integration for meshfree Mindlin-Reissner plate formulation, Comput. Meth. Appl. Mech. Engrg. 193 (2004) 1065-1083.

[35] D. Wang, Y, Sun, A Galerkin meshfree method with stabilized conforming nodal integration for geometrically nonlinear analysis of shear deformable plates, Int. J. Comput. Meth. 8 (2011) 685-670.

[36] J.S. Chen, C.T. Wu, S. Yoon, Y. You, A stabilized conforming nodal integration for Galerkin meshfree methods, Int. J. Numer. Meth. Eng. 50 (2001) 435-466.

[37] J.S. Chen, S. Yoon, C.T. Wu, Non-linear version of stabilized conforming nodal integration for Galerkin mesh-free methods, Int. J. Numer. Meth. Eng. 53 (2002) 2587-2615.

[38] D. Wang, J.S. Chen, A Hermite reproducing kernel approximation for thin-plate analysis with sub-domain stabilized conforming integration, Int. J. Numer. Meth. Eng. 74 (2008) 368-390.

[39] D. Wang, Z. Lin, Free vibration analysis of thin plates using Hermite reproducing kernel Galerkin meshfree method with sub-domain stabilized conforming integration, Comput. Mech. 46 (2010) 703-719.

[40] D. Wang, Z. Lin, Dispersion and transient analyses of Hermite reproducing kernel Galerkin meshfree method with sub-domain stabilized conforming integration for thin beam and plate structures, Comput. Mech. 48 (2011) 47-63.

[41] D. Wang, Z. Lin, A comparative study on the dispersion properties of HRK and RK meshfree approximations for Kirchhoff plate problem, Int. J. Comput. Meth. 9 (2012) 1240015.

[42] D. Wang, H. Peng, A Hermite reproducing kernel Galerkin meshfree approach for buckling analysis of thin plates, Comput. Mech. 51 (2013) 1013-1029.

[43] D. Wang, C. Song, H.K. Peng, A circumferentially enhanced Hermite reproducing kernel meshfree method for buckling analysis of Kirchhoff-Love cylindrical shells, Int. J. Struct. Stabil. Dynam. 15 (2015) 1450090.

[44] D. Wang, J. Wu, An efficient nesting sub-domain gradient smoothing integration algorithm with quadratic exactness for Galerkin meshfree methods, Comput. Methods Appl. Mech. Engrg. 298 (2016) 485-519.

[45] D. Wang, J. Wu, An inherently consistent reproducing kernel gradient smoothing framework toward efficient Galerkin meshfree formulation with explicit quadrature, Comput. Methods Appl. Mech. Engrg. 349 (2019) 628-672.

[46] S. Sadamoto, S. Tanaka, S. Okazawa, Elastic large deflection analysis of plates subjected to uniaxial thrust using meshfree Mindlin-Reissner formulation, Comput. Mech. 52 (2013) 1313-1330.

[47] K. Yoshida, S. Sadamoto, Y. Setoyama, S. Tanaka, T.Q. Bui, C. Murakami, D. Yanagihara, Meshfree flat-shell formulation for evaluating linear buckling loads and mode shapes of structural plates, J. Mar. Sci. Tech. 22 (2017) 501-512.

[48] M. Ozdemir, S. Tanaka, S. Sadamoto, T.T. Yu, T.Q. Bui, Numerical buckling analysis for flat and cylindrical shells including through crack employing effective reproducing kernel meshfree modeling, Eng. Anal. Bound. Elem. 97 (2018) 55-66.

[49] J.S. Chen, H.P. Wang, New boundary condition treatments in meshfree computation of contact problems, Comput. Methods Appl. Mech. Engrg. 187 (2000) 441-468.

[50] S. Sadamoto, S. Tanaka, K. Taniguchi, M. Ozdemir, T.Q. Bui, C. Murakami, D. Yanagihara, Buckling analysis of stiffened plate structures by an improved meshfree flat shell formulation, Thin-Walled Struct. 117 (2017) 303-313.

[51] M. Ozdemir, S. Sadamoto, S. Tanaka, S. Okazawa, T.T. Yu, T.Q. Bui, Application of 6-DOF meshfree modeling to the linear buckling analysis of stiffened plates with curvilinear surface, Acta Mech. 229 (2018) 4995-5012.

[52] D. Organ, M. Fleming, T. Terry, T. Belytschko, Continuous meshless approximations for nonconvex bodies by diffraction and transparency, Comput. Mech. 18 (1996) 225-235.

[53] P. Joyot, J. Trunzler, F. Chinesta, Enriched reproducing kernel approximation: Reproducing functions with discontinuous derivatives, Lecture Notes in Comput. Sci. and Eng. 43 (2005) 93-107.

[54] S. Tanaka, H. Suzuki, S. Sadamoto, M. Imachi, T.Q. Bui, Analysis of cracked shear deformable plates by an effective meshfree plate formulation, Eng. Fract. Mech. 144 (2015) 142-157.

[55] S. Tanaka, H. Suzuki, S. Sadamoto, S. Sannomaru, T.T. Yu, T.Q. Bui, J-integral evaluation for 2D mixed-mode crack problems employing a meshfree stabilized conforming nodal integration method, Comput. Mech. 58 (2016) 185-198.

[56] S. Tanaka, H. Suzuki, S. Sadamoto, S. Okazawa, T.T. Yu, T.Q. Bui, Accurate evaluation of mixed-mode intensity factors of cracked shear-deformable plates by an enriched meshfree Galerkin formulation, Arch. Appl. Mech. 87 (2017) 279-298.

[57] T. Dirgantara, M.H. Aliabadi, Boundary element analysis of assembled plate structures, Comm. Numer. Meth. Eng. 17 (2001) 749-760.

[58] T. Dirgantara, M.H. Aliabadi, Stress intensity factors for cracks in thin plates, Eng. Fract. Mech. 69 (2002) 1465-1486.

[59] H. Ishikawa, A finite element analysis of stress intensity factors for combined tensile and shear loading by only a virtual crack extension, Int. J. Fract. 16 (1980) R243-246.

[60] I.S. Raju, K.N. Shivakumar, An equivalent domain integral method in the two-dimensional analysis of mixed mode crack problems, Eng. Fract. Mech. 37 (1990) 707-725.

[61] W. Kanok-Nukulchai, A simple and efficient finite element for general shell analysis, Int. J. Numer. Meth. Eng. 14 (1979) 179-200.

[62] Y. Murakami, Stress intensity factors handbook: Vol. 2, Pergamon Press, Oxford, 1987.

[63] M. Isida, Effect of width and length on stress intensity factors of internally cracked plates under various boundary conditions, Int. J. Frac. 7 (1971) 301-316.

[64] MSC. Marc. Volume A: theory and user information, version 2001. Revision April 2001. MSC Software Corporation, 2001.

[65] Abaqus-Inc, Analysis user's manual, version 6.12. Providence. RI (USA): Dassault Systems Simulia Corp, 2012.

[66] O.L. Bowie, Solutions of plane crack problems by mapping technique (Chapter 1), Mechanics of fracture (edited by G.C. Sih), 1-55, Noordhoff, International Publishing, Leyden, The Netherlands, 1972.